gene could be inserted into Tn5, which would aid in the detection of recombinant viruses and could be used as a probe for tracing the extent of viral infection in the host. Thus, it appears that the Tn5 mutagenesis procedure described here will be applicable for analyzing large numbers of genes in HSV-1, and in other animal viruses with large complex genomes.

REFERENCES AND NOTES

1. R. J. Whitley, in *The Herpesviruses*, B. Roizman, Ed. (Plenum, New York, 1985), vol. 3, pp. 1–44.
2. H. J. Field and P. Wildy, *J. Hyg.* **81**, 267 (1978); A. E. Sears, I. A. Halliburton, B. Merignier, S. Silver, B. Roizman, *J. Virol.* **55**, 338 (1985); G. Kumel, H. C. Kaerner, M. Levine, C. H. Schröder, J. C. Glorioso, *ibid.* **56**, 930 (1985).
3. F. J. deBruijn and J. R. Lupski, *Gene* **27**, 131 (1984); D. F. Berg and C. M. Berg, *Biotechnology* **1**, 417 (1983).
4. D. J. McGeoch, A. Dolan, S. McDonald, F. J. Rixon, *J. Mol. Biol.* **181**, 1 (1985); F. J. Rixon and D. J. McGeoch, *Nucleic Acids Res.* **13**, 953 (1985).
5. L. E. Post and B. Roizman, *Cell* **25**, 227 (1981); R. Longnecker and B. Roizman, *J. Virol.* **58**, 583 (1986).
6. F. L. Homa *et al.*, *Mol. Cell. Biol.* **6**, 3652 (1986).
7. M. C. Frame *et al.*, *J. Gen. Virol.* **67**, 745 (1986).
8. L. E. Post and B. Roizman, *Cell* **25**, 227 (1981).
9. F. J. Jenkins, M. J. Casadaban, B. Roizman, *Proc. Natl. Acad. Sci. U.S.A.* **82**, 4773 (1985).
10. M. J. Murchie and D. J. McGeoch, *J. Gen. Virol.* **62**, 1 (1982).
11. R. J. Watson, J. H. Weiss, J. S. Salstrom, L. W. Enquist, *Science* **218**, 381 (1982); G. T. Y. Lee, M. F. Para, P. G. Spear, *J. Virol.* **43**, 41 (1982); M. C. Frame, H. S. Marsden, D. J. McGeoch, *J. Gen. Virol.* **67**, 745 (1986).
12. M. C. Frame, D. J. McGeoch, F. J. Rixon, A. C. Orr, H. S. Marsden, *Virology* **150**, 321 (1986).
13. D. J. McGeoch and A. J. Davison, *Nucleic Acids Res.* **14**, 1765 (1986).
14. P. A. Johnson, C. MacLean, H. S. Marsden, R. G. Dalziel, R. D. Everett, *J. Gen. Virol.* **67**, 871 (1986).
15. Plasmids were constructed by F. L. Homa, R. M. Sandri-Goldin, and L. E. Holland in our laboratories.
16. G. Kumel *et al.*, *J. Virol.* **56**, 930 (1985).

17. Supported by Public Health Service grants AI18228, GM34534, and RR00200 from the National Institutes of Health. P.C.W. was supported by the Dental Research Institute Associated Program from the Office of Vice President for Research and by NIH postdoctoral fellowship 1 F32 GM11718-01. We thank D. Clewell for providing phages and bacterial strains, and C. Chrisp, D. Cole, S. Highlander, and especially F. Homa for technical assistance and helpful advice.

22 December 1986; accepted 3 March 1987

Distribution of Cones in Human and Monkey Retina: Individual Variability and Radial Asymmetry

CHRISTINE A. CURCIO, KENNETH R. SLOAN, JR., ORIN PACKER, ANITA E. HENDRICKSON, ROBERT E. KALINA

The distribution of photoreceptors is known for only one complete human retina and for the cardinal meridians only in the macaque monkey retina. Cones can be mapped in computer-reconstructed whole mounts of human and monkey retina. A 2.9-fold range in maximum cone density in the foveas of young adult human eyes may contribute to individual differences in acuity. Cone distribution is radially asymmetrical about the fovea in both species, as previously described for the distribution of retinal ganglion cells and for lines of visual isosensitivity. Cone density was greater in the nasal than in the temporal peripheral retina, and this nasotemporal asymmetry was more pronounced in monkey than in human retina.

THE TOPOGRAPHIC DISTRIBUTION, size, and packing geometry of photoreceptors contribute to the functional grain of the primate retina. Most of what is known about these variables in the human retina comes from the classic study of Østerberg (*1*), but sampling gaps in that study have left our understanding of photoreceptor topography incomplete. In the fovea, the region responsible for acute vision, only a small strip of the temporal horizontal meridian was examined. A large portion of the inferior peripheral retina was not available for analysis. Furthermore, because only one retina was studied, variability in either the overall pattern or absolute values of the photoreceptor map remains unknown. Several estimates exist for the maximum density of cones in the young adult fovea (*2, 3*), but each of these histological studies also included only one eye.

Because the Old World macaque monkey is used widely as a model of the human visual system, it is important to compare macaque and human retinas by similar methods. There is considerable information on behaviorally measured visual development (*4*) in *Macaca nemestrina*, but little information about retinal anatomy. Topographic data are available for the retina of *M. mulatta* and *M. fascicularis*, but most of the data are confined to the fovea (*3, 5*) or the horizontal and vertical meridians (HM and VM) (*6, 7*). As far as we know, no complete topographic description is available for any macaque retina.

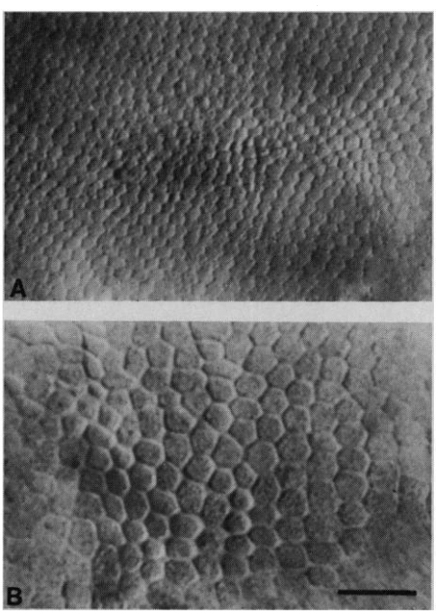

Fig. 1. Optical sections through cone inner segments at the center of the fovea in human retinas with (**A**) high peak density (H1) and (**B**) low peak density (H2). Micrographs are the same dimensions as the counting field. Bar, 10 μm.

We have developed tissue and computational techniques (*8, 9*) to facilitate the collection and analysis of topographic data from four human and two *M. nemestrina* retinas. Our data represent the first photoreceptor maps for the human retina since Østerberg's study and the first ever for the monkey retina. We describe the distribution of cones in these two species, extending the previously described topography and providing new evidence for radial asymmetry and individual variability.

Four human retinas (H1 to H4) were obtained from eye bank donors under 45 years of age without history of eye disease. Eyes were fixed in phosphate-buffered 4% paraformaldehyde and 0.5% glutaraldehyde within 3 hours of death. Eyes were inspected under the dissecting microscope to exclude ocular disease and postmortem retinal folds. Two *M. nemestrina* eyes (M1 and M2), obtained from the Regional Primate Research Center, were enucleated under deep barbiturate anesthesia. The eyes were injected intravitreally with phosphate-buffered 4% paraformaldehyde and immersed in the same fixative within 10 minutes after being removed (*10*).

Eyes were trisected into a belt containing

C. A. Curcio and A. E. Hendrickson, Departments of Biological Structure and Ophthalmology, University of Washington, Seattle, WA 98195.
K. R. Sloan, Jr., Department of Computer Science, University of Washington, Seattle, WA 98195.
O. Packer, Department of Psychology, University of Washington, Seattle, WA 98195.
R. E. Kalina, Department of Ophthalmology, University of Washington, Seattle, WA 98195.

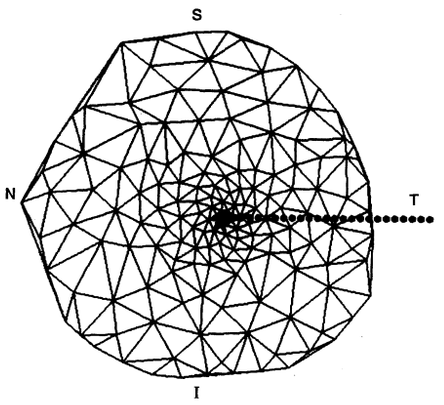

Fig. 2. Sampling scheme used for retinas of H4 and M2. Four retinal quadrants (N, nasal; T, temporal; S, superior; I, inferior) are denoted. Locations of data points are connected into a mesh by Delaunay triangulation (*23*) and displayed in polar azimuthal equidistant projection. The fovea was more densely sampled than the periphery, with a rectangular grid of 9 to 16 adjacent fields in the center of the foveola. Counts were also made in the far periphery at the first fields posterior to the ora serrata where rods and cones were clearly recognizable. Sampling schemes for other eyes were based on a hexagonal grid whose spacing increased with eccentricity from the fovea rather than the illustrated spiral. Final locations of points in individual sampling grids deviated slightly from the ideal pattern. The line of dots along the temporal horizontal meridian illustrates how the meridian resampling program used to generate Fig. 3 traces a path along the retinal surface. At each dot, a weighted mean of densities at the vertices of each containing triangle is calculated.

the fovea, optic disk and horizontal meridian, an inferior cap, and a superior cap. The retina was detached from the retinal pigment epithelium, flattened on a plastic slide, cleared and coverslipped with dimethyl sulfoxide or glycerine (*8*). Nomarski differential interference contrast optics allow us to view optical sections at different levels along the long axis of photoreceptors (Fig. 1). Rod and cone inner segments are easily distinguished at their presumed entrance aperture, a level just sclerad to the external limiting membrane (*11*). Photoreceptors were counted in whole mounts, through the use of a computer-video-microscope system, at locations determined by a sampling grid whose density decreased smoothly with eccentricity from the fovea (Fig. 2) (*12*).

We developed a digital model of the retina that consists of locations on the retinal sphere (*13*) indexed by spherical coordinates and associated attributes such as photoreceptor density. Our software transforms the data from locations in the whole mount back to spherical coordinates by using the fovea and optic disk as reference points and retinal vasculature to connect across cut edges. Programs display color-coded density maps in the polar azimuthal equidistant projection. Other programs resample the digital model and plot photoreceptor density along any meridian (Figs. 2 and 3).

The distribution of cones in both human and monkey retina peaked in the center of the fovea, with cone density falling off sharply with eccentricity as previously described (*1, 5–7*). Comparison of the cone distribution in eyes H1 to H4 and for the eye examined by Østerberg (Fig. 3) reveals extensive overlap in the peripheral retina and a marked variability in the fovea that was qualitatively obvious in the tissue (Fig. 1). In our sample, peak foveal cone density in a 54 by 37 μm field ranged from 96,900 cones per square millimeter (H2) to 281,000 mm^{-2} (H1), a 2.9-fold range. Mean peak density was 161,900 mm^{-2}, whereas Østerberg's original estimate was 147,000 mm^{-2}. In the monkey eye, peak cone densities were 188,000 (M1) and 190,000 mm^{-2} (M2). Estimates of peak density depend on the size of the counting field. Our values were 10 to 20% higher for all eyes when determined for a 35% smaller counting field that included less surrounding area of lower density.

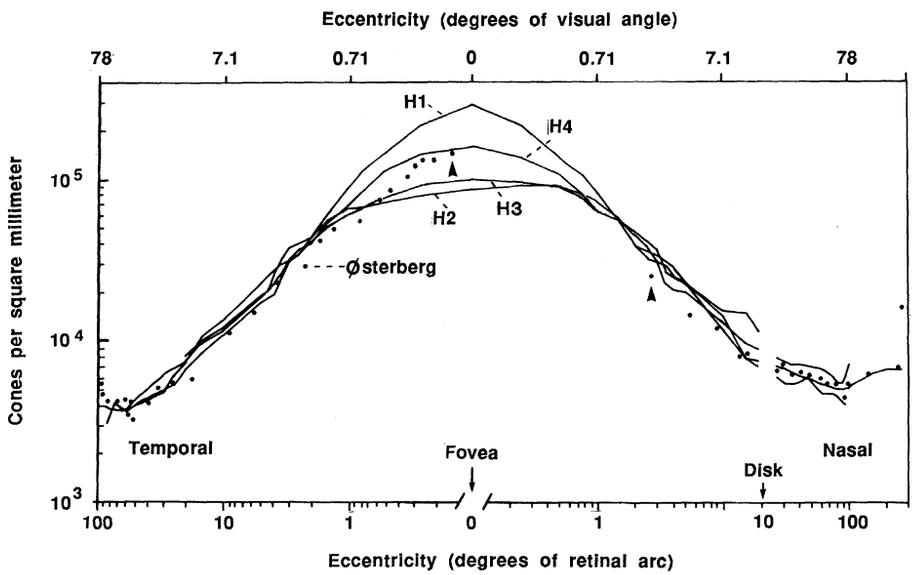

Fig. 3. Comparison of cone distribution along the horizontal meridian in human subjects H1 to H4 (interpolated as in Fig. 2) and in the eye analyzed by Østerberg (with his original data points, indicated by dots). The distribution of Østerberg's data points is virtually identical to a resampled version created by our programs in the manner used for H1 to H4. Østerberg's sampling gap on the nasal side of the fovea (arrowheads) causes an interpolation artifact. Several of his points in the far periphery have been deleted for illustrative clarity. This log-log plot accentuates differences at low eccentricities near the fovea and low densities in the periphery (*13*).

Density contour plots (Fig. 4, A and B) revealed that the distribution of cones in the primate retina is radially asymmetrical around the fovea in two ways.

1) Isodensity contours were elliptical and aligned with the HM, indicating that cone density falls off more rapidly along the VM than along the HM. In three human eyes this ellipticity was present in the fovea, where the axial ratio (HM:VM) of the contour at half-maximum density was 1.2 to 1.4 (Fig. 4B). In H4 and in both monkeys, foveal isodensity contours were virtually circular (*14*). In the far periphery of human retina (Fig. 4C), low-density contours (under 5000 mm^{-2}) expanded away from the nasal HM into the superior and inferior retina, whereas such contours in the monkey eye remained elliptical or narrowly open at the nasal end.

2) We observed, as have others (*1, 6*), that cone density is higher in the nasal than in the temporal retina in both human and monkey. However, the nasotemporal asymmetry was not consistently present until outside the optic disk, as illustrated by a shift of the centers of isodensity contours toward the nasal side at higher eccentricities. This asymmetry was much more pronounced in the monkey, where cone density decreased more slowly nasally than in other retinal quadrants. Thus, cones in the nasal retina increasingly exceeded those at corresponding eccentricities in the temporal retina up to a maximum difference of 300% (M1) and 250% (M2) in the far periphery. In contrast, cones in the human nasal retina exceeded those in the temporal retina by only 10 to 40% in H1, H2, and H3 and 40 to 70% in H4. A slight increase in cone density (*1*) in the far nasal periphery was noted in two human eyes (H2 and H4).

A new finding in the human retina was the striking degree of variability in maxi-

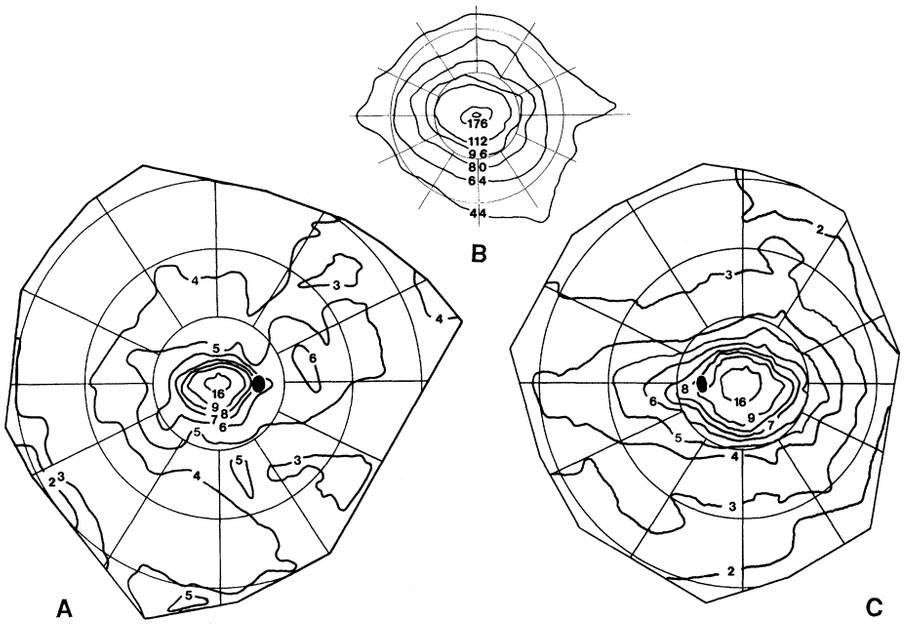

Fig. 4. Polar azimuthal equidistant projections of contour maps showing distribution of cones in periphery (**A**) and fovea (**B**) of human H1 and periphery (**C**) of monkey M1. In the overlying grid, lines of isoeccentricity are at 30° of arc (A and C) and at 1° (B) on the retinal sphere. The black oval denotes the optic disk. Contour lines are at increments of 1,000 mm^{-2} in (A) and (C) and at 16,000 mm^{-2} in (B).

mum cone density in the fovea of young, presumably normal adult eyes. Much less variability was observed for peripheral cones and rods (*15*) in the same specimens and for peak cone density in more rapidly fixed monkey fovea. These results cannot be due to either variation in processing-induced changes in overall tissue volume, which caused a 2 to 12% increase in retinal area in another series of similarly prepared specimens (*8*), or variation in the three-dimensional topography of the external fovea (*12*). The all-cone fovea is more vulnerable to the degenerative effects of postmortem delay before fixation than is peripheral retina (*16*), so that differential fixation-induced changes in tissue volume remain a possible explanation. We cannot determine the magnitude of this effect without information about the dimensions of the fovea before death. We did, however, screen out eyes with macroscopically obvious foveal edema or folds. Less variability (a 25% range) has been observed in laser interferometric estimates of maximum cone density of the human fovea in vivo (*17*). This discrepancy may be due to the more rigorous criteria for refractive error and acuity used in selecting psychophysical observers.

Variability in foveal cone density may reflect differences in the rate, timing, or extent of the developmental migration of cones toward the foveal center (*16, 18*). It may also be compensatory for variability in the optical constants of the eye and the magnification of images on the retina. Individual differences in foveal architecture may contribute to individual differences in behavioral acuity (*19*) along with optical and stimulus factors. We plan to test this idea with a similar analysis of retinas from persons whose visual function is more completely documented.

The distribution of cones is radially asymmetrical about the fovea, as is the distribution of retinal ganglion cells in the primate retina (*6, 20*) and lines of constant detection and resolution sensitivity in the visual field (*21*). Higher cone densities in the nasal and superior retinal quadrants were observed by Østerberg (*1*). Our more intensive sampling of the central retina shows that some horizontal elongation of isodensity contours may appear in the fovea itself, whereas nasotemporal asymmetry is not present until a more peripheral location is reached, which suggests that these aspects of cone distribution may be dissociated. A nasotemporal difference in the optical density of foveal cone photopigments (*22*) may be attributable to cone morphology or photopigment concentration rather than by cone number.

Our approach toward systematically mapping human and monkey retinas will help distinguish variant and invariant features of primate retinal cell distributions. We have shown that cone topography in the monkey is qualitatively similar to that in the human over much of the retina and that it should therefore be possible to predict human retinal topography from monkey eyes used in invasive experiments. The extension of our approach to retinal development, aging, and pathology will ultimately provide a firmer anatomical basis for theories of vision invoking the photoreceptor mosaic.

REFERENCES AND NOTES

1. G. A. Østerberg, *Acta Ophthalmol.* (*Suppl.* **6**) 1 (1935).
2. H. Hartridge, *Recent Advances in the Physiology of Vision* (Blakiston, Philadelphia, 1935).
3. W. H. Miller, *Handbook of Sensory Physiology,* vol. 7, part 6, *Comparative Physiology and Evolution of Vision in Invertebrates,* A, *Invertebrate Photoreceptors,* H. Autrum, Ed. (Springer-Verlag, Berlin, 1979), pp. 69–144.
4. R. G. Boothe, V. Dobson, D. Y. Teller, *Annu. Rev. Neurosci.* **8**, 495 (1985).
5. B. Borwein, D. Borwein, J. Medeiros, J. W. McGowan, *Am. J. Anat.* **159**, 125 (1980).
6. V. H. Perry and A. Cowey, *Vision Res.* **25**, 1795 (1985).
7. E. T. Rolls and A. Cowey, *Exp. Brain Res.* **10**, 298 (1970); C. K. Adams, J. M. Perez, M. N. Hawthorne, *Invest. Ophthalmol.* **13**, 885 (1974); F. M. de Monasterio *et al.*, *Invest. Ophthalmol. Visual Sci.* **26**, 289 (1985).
8. C. A. Curcio, O. Packer, R. E. Kalina, *Vision Res.* **27**, 9 (1987).
9. K. R. Sloan, Jr., D. Meyers, C. A. Curcio, *Proceedings: Graphics Interface '86/Vision Interface '86* (Canadian Information Processing Society, Toronto, 1986), pp. 385–389.
10. The four humans studied and causes of death were: a 44-year-old female, subarachnoid hemorrhage (H1); a 27-year-old male, multiple trauma (H2); a 35-year-old female, brain tumor (H3); and a 34-year-old male, head injury and respiratory arrest (H4). The two monkeys were a 6.5-year-old male (M1) and a 13.5-year-old female (M2).
11. W. H. Miller and G. Barnard, *Vision Res.* **23**, 1365 (1983).
12. C. A. Curcio and K. R. Sloan, Jr., *Anat. Rec.* **214**, 329 (1986). Rods and cones were counted from video images of tissue at each location in the sampling grid, with a 130- by 88-μm counting field used for peripheral cones and a 54- by 37-μm field for foveal cones and all rods. The three-dimensional topography of the external foveal pit was evident and variable in slope. Cell counts on sloping tissue in this area were made at different levels of focus so that density is expressed in terms of its projection onto the plane of the counting field. Densities expressed in terms of number of cones per square millimeter of sloping tissue were lower by 1.8 and 15% (H4 and H1, respectively).
13. To normalize data from different sized eyes, we considered the retina to be a sphere whose diameter was its equatorial ocular diameter less its scleral thickness. The fovea was at the pole, and the horizontal meridian passed through the fovea and the center of the optic disk. Eccentricity was expressed in terms of degrees of retinal arc, the average length of which was 0.199 mm/deg (range 0.189 to 0.207) for the human eyes. These degrees are smaller than degrees of eccentricity in the visual field because retinal radius is less than posterior nodal distance. Visual degrees (Fig. 3) were estimated from a schematic eye [N. Drasdo and C. W. Fowler, *Br. J. Ophthalmol.* **58**, 709 (1974)], which provides a retinal magnification factor of 280 μm per degree of visual angle, or 1.4° of retinal arc per degree of visual angle, at the fovea.
14. Eye H2 had an unusually organized fovea, with multilobed isodensity contours and the point of highest cone density displaced 100 μm superior and temporal to the center of the external foveal pit. There were some slight folds on the vitreal surface of the foveal depression that did not agree with the pattern of isodensity contours. No obvious explanation for this finding was apparent from available medical records.
15. Maximum numbers of rods per square millimeter in eyes mapped far enough from the fovea to include the rod maximum were 188,000 (H1), 157,900 (H3), and 181,000 (H4).
16. A. E. Hendrickson and C. Yuodelis, *Ophthalmology* **91**, 603 (1984); C. Yuodelis and A. E. Hendrickson, *Vision Res.* **26**, 847 (1986).
17. D. R. Williams, *Vision Res.* **25**, 195 (1985); personal communication.
18. A. E. Hendrickson and C. Kupfer, *Invest. Ophthalmol.* **15**, 746 (1976).
19. M. L. Rubin and G. L. Walls, *Fundamentals of Visual Science* (Thomas, Springfield, IL, 1969), p. 178.
20. G. A. Van Buren, *The Retinal Ganglion Cell Layer* (Thomas, Springfield, IL, 1963); J. Stone and E.

Johnston, *J. Comp. Neurol.* **196**, 205 (1981).
21. T. Wertheim, *Z. Psychol. Physiol.* **7**, 172 (1894); L. O. Harvey and E. Poppel, *Am. J. Optom.* **49**, 748 (1972); C. A. Johnson, J. L. Keltner, F. Balestrery, *Vision Res.* **18**, 1217 (1978); I. Lie, *ibid.* **20**, 967 (1980).
22. P. E. Kilbride, J. S. Read, G. A. Fishman, M. Fishman, *Vision Res.* **23**, 1341 (1983).
23. F. P. Preparata and M. I. Shamos, *Computational Geometry: An Introduction* (Springer-Verlag, New York, 1985).
24. Supported by NIH grants EY06109 to C.A.C., EY04536 and EY01208 to A.E.H., the Lions Sight Conservation Foundation of Washington–Northern Idaho, and NSF grant DCR-8505713 to K.R.S. We thank D. J. McCulloch for technical assistance, D. Meyers for programming support, and the personnel of the Lions Eye Bank and the Regional Primate Research Center at the University of Washington for obtaining tissue.

3 September 1986; accepted 23 December 1986

β1–6 Branching of Asn-Linked Oligosaccharides Is Directly Associated with Metastasis

JAMES W. DENNIS,* SUZANNE LAFERTÉ, CAROL WAGHORNE, MARTIN L. BREITMAN, ROBERT S. KERBEL

Neoplastic transformation has been associated with a variety of structural changes in cell surface carbohydrates, most notably increased sialylation and β1–6–linked branching of complex-type asparagine (Asn)-linked oligosaccharides (that is, –GlcNAcβ1–6Manα1–6Manβ1–). However, little is known about the relevant glycoproteins or how these transformation-related changes in oligosaccharide biosynthesis may affect the malignant phenotype. Here it is reported that a cell surface glycoprotein, gp130, is a major target of increased β1–6–linked branching and that the expression of these oligosaccharide structures is directly related to the metastatic potential of the cells. Glycosylation mutants of a metastatic tumor cell line were selected that are deficient in both β1–6 GlcNAc transferase V activity and metastatic potential in situ. Moreover, induction of increased β1–6 branching in clones of a nonmetastatic murine mammary carcinoma correlated strongly with acquisition of metastatic potential. The results indicate that increased β1–6–linked branching of complex-type oligosaccharides on gp130 may be an important feature of tumor progression related to increased metastatic potential.

ONE OF THE MORE CONSISTENTLY observed alterations following neoplastic transformation is a shift toward the synthesis and expression of larger Asn-linked oligosaccharides (*1–5*). Such changes have been detected in both rodent (*1–3*) and human tumor cells (*5*) transformed by chemical mutagens (*1*), oncogenic viruses (*2*), or by transfection with DNA obtained from neoplastic cells (*3*). In a number of studies the change in size has been attributed to an increase in sialic (neuraminic) acid content of the structures (*4–6*). More recently, rodent cells transformed with polyoma virus (*7*) or cells transfected with activated H-*ras* oncogenes (*8*) have been shown to be more highly branched at the trimannosyl core of Asn-linked glycans because of the addition of β1–6–linked lactosamine antennae (that is, galβ1–4GlcNAcβ1–6). Since many of the lactosamine antennae are substituted with sialic acid, increased branching may also contribute to the transformation-related increase in sialic acid. Branching of complex Asn-linked oligosaccharides to produce tri-, tri′-, and tetra-antennary structures appears to depend on the action of UDP-GlcNAc:α-D–mannoside β1,4*N*-acetylglucosaminyltransferase (that is, GlcNAc transferase IV) and UDP-GlcNAc:α-D–mannoside β1,6*N*-acetylglucosaminyltransferase (that is, GlcNAc transferase V) (*9*) (Fig. 1). After the action of the GlcNAc transferases, processing is completed by the addition of galactose and sialic acid to produce the common sialyllactosamine antennae. Yamashita *et al.* compared six GlcNAc transferase activities and found only transferase V was elevated two times more than normal in polyoma virus–transformed BHK cells (*10*).

As a first approach to determine whether expression of specific oligosaccharide structures on malignant cells contribute to their tumorigenic or metastatic behavior, we isolated glycosylation mutants of the highly metastatic, murine tumor cell line called MDAY-D2 (*11*). For example, the class 1 genotype was consistently nonmetastatic in both syngeneic and immunosuppressed nude mice. The biochemical basis of this mutation appeared to be a deficiency in the transport of uridine diphosphate (UDP)–galactose into the Golgi apparatus, and, consequently, Asn-linked oligosaccharides lacked the typical sialylated lactosamine antennae (*12*). By taking advantage of the hypersensitivity of the class 1 cells to BSII lectin from *Bandeirea simplicifolia*, we were able to select single-step revertants that simultaneously regained the sialylated lactosamine antennae and the highly metastatic phenotype, thereby showing a direct association between the glycosylation defect and loss of metastatic potential in these cells (*13*).

Since the class 1 mutation also inhibited ganglioside biosynthesis (*14*), these studies did not indicate which classes of glycoconjugates were required for expression of the metastatic phenotype. We therefore selected glycosylation mutants with defects limited to Asn-linked oligosaccharide biosynthesis. The class 3 mutants of MDAY-D2 cells were selected in medium containing leukoagglutinin (L-PHA) and BSII lectin; the latter lectin was added to eliminate class 1 mutants (*13*). The choice of L-PHA for mutant selection was based on the known binding specificity of the lectin for tri′- and tetra-antennary complex-type oligosaccharides (*15*). L-PHA binding requires the β1–6–linked lactosamine antennae and has recently been used to detect these structures in transformed cells (*8*). Two clones, KBL1 and KBL2, with identical lectin sensitivity profiles were isolated, and although the mutants were highly tumorigenic, their metastatic potential was dramatically reduced (Table 1). Compared to MDAY-D2, the mutants were poorly metastatic when injected by either intravenous or subcutaneous routes.

The structural changes in the class 3 lectin resistant mutants could be deduced from the lectin staining of glycoproteins separated by

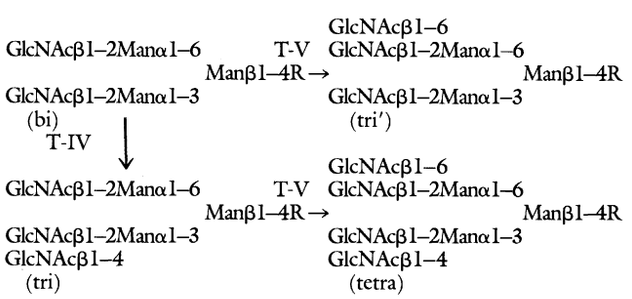

Fig. 1. GlcNAc transferases IV and V initiate the peripheral antennae in tri-, tri′- and tetra-antennary complex-type oligosaccharides. Only structures with the β1–6–linked antennae and further substitutions of galactose bind L-PHA (*15*). R = GlcNAcβ1–4GlcNAc1-Asn.

Division of Cancer and Cell Biology, Mount Sinai Hospital Research Institute, 600 University Avenue, Toronto, and Department of Medical Genetics, University of Toronto, Ontario, Canada M5G 1X5.

*To whom correspondence should be addressed.